Bioactive Materials 9 (2022) 554–565

Contents lists available at ScienceDirect

Bioactive Materials

journal homepage: www.sciencedirect.com/journal/bioactive-materials

A tumor-penetrable drug nanococktail made from human histones for interventional nucleus-targeted chemophotothermal therapy of drug-resistant tumors

Jianquan Guo [b,1], Dongsheng Tan [a,1], Chenmei Lou [a,1], Shiying Guo [a], Xing Jin [a], Haijing Qu [a], Lijia Jing [a,*], Sijin Li [b,**]

[a] Key Laboratory of Saline-alkali Vegetation Ecology Restoration, Ministry of Education, College of Life Science, Northeast Forestry University, Harbin, 150040, China
[b] Department of Nuclear Medicine, First Hospital of Shanxi Medical University, Taiyuan, 030001, Shanxi, China

ARTICLE INFO

Keywords:
Human histones
Chemotherapy
Photothermal therapy
Nuclear targeting
Localized intervention
Drug resistant tumor

ABSTRACT

Nanoparticle-based chemophotothermal therapy (CPT) is a promising treatment for multidrug resistant tumors. In this study, a drug nanococktail of DIR825@histone was developed by employing doxorubicin (DOX), NIR dye IR825 and human histones for interventional nucleus-targeted CPT of multidrug resistant tumors with an interventional laser. After localized intervention, DIR825@histone penetrated tumor tissues by transcytosis, efficiently entered tumor cells and targeted the cell nuclei. DIR825@histone also exhibited good photothermal performance and thermal-triggered drug release. Efficient multidrug resistant tumor inhibition was achieved by enhanced CPT sensitization and MDR reversion via nuclear targeting. Moreover, an interventional laser assisted DIR825@histone in inhibiting multidrug resistant tumors by promoting the sufficient delivery of laser energy inside the tumor while reducing skin injury. Therefore, DIR825@histone together with this interventional nucleus-targeted CPT strategy holds great promise for treating multidrug resistant tumors.

1. Introduction

Chemotherapy is an indispensable treatment for tumors. However, its efficiency is often limited by multidrug resistance (MDR) [1]. Clinically, MDR is mainly induced by the overexpression of P-glycoprotein (P-gp) encoded by the MDR1 gene, which can weaken chemotherapy efficacy by active drug efflux [2–4]. Photothermal therapy (PTT), which ablates tumors by converting a near-infrared (NIR) laser into heat through photoabsorbers, has gained remarkable interest in the field of oncology [5–7]. In addition to tumor ablation, PTT can boost cellular drug uptake and reverse MDR by inhibiting P-gp [8]. To date, nanoparticles (NPs) with chemophotothermal therapeutic (CPT) potential have been widely explored as drug nanococktails to treat multidrug resistant tumors due to their remarkable spatial/temporal synergistic effects [9–13].

Unlike normal tissues, solid tumors typically have abnormal vasculature and relatively high interstitial fluid pressure, which often leads to the heterogeneous and insufficient tumor absorption of nanoparticulate drugs [14–16]. In addition, the fast blood clearance of NPs by reticuloendothelial system (RES) remains a great challenge to adequately delivering nanoparticulate drugs to the tumor site [17]. Compared to whole body medication, localized interventions have recently gained attention for accurately delivering tumor medications [18]. With local intervention, the tumor-targeted delivery of nanoparticulate drugs can be easily achieved, and systemic toxicity can be avoided [19,20]. For PPT treatment, interventional laser devices can overcome the low penetration depth of NIR lasers for heating deep-seated tumors [21,22]. Therefore, an interventional CPT strategy that employs the localized delivery of NIR laser energy and drug nanococktails may be advantageous for treating multidrug resistant tumors with different locations and features.

In addition to the adequate delivery of drug nanococktails and laser energy to the tumor site, intracellular targets for synergistic chemotherapy, tumor ablation and MDR reversion are critical for improved

Peer review under responsibility of KeAi Communications Co., Ltd.
* Corresponding author.
** Corresponding author.
E-mail address: jinglijia@nefu.edu.cn (L. Jing).
[1] These authors contributed equally.

https://doi.org/10.1016/j.bioactmat.2021.07.018
Received 11 December 2020; Received in revised form 23 June 2021; Accepted 19 July 2021
Available online 31 July 2021

CPT treatment of multidrug resistant tumors. The nucleus is the most important part of the cell. Since most cancer drugs are DNA toxic [23,24], NPs capable of nucleus-targeted chemotherapy are highly efficacious for the inhibition of multidrug resistant tumors [25–27]. For PTT of tumors, improved therapeutic outcomes can be achieved by targeting the photothermal effect to the nucleus of tumor cells [28–30]. Moreover, from a biomechanical perspective, the nucleus is a potential PTT target for MDR reversion since the nucleus is the site where drug resistance genes undergo transcription. These findings remind us that targeting the CPT effect at the nucleus of tumor cells is more efficacious for multidrug resistant tumor inhibition.

Currently, several nanocarriers capable of nucleus-targeting ability have been explored. However, most of them require complicated synthesis processes, which is an obstacle to their widespread application. Histones are functional proteins in the chromatin of cells [31,32]. Compared with current carrier materials, histones have obvious advantages in constructing nucleus-targeted carriers. Histones are endogenous substances, which can be degraded and metabolized by the human body. In addition, the amino acid sequence of histones contains a nuclear localization sequence, which can be recognized by the nuclear pore complex and transported to the nucleus. Inspired by this activity, we used human histones for the first time to fabricate nucleus-targeted nanococktails. The nanococktail of DIR825@histone was developed by employing doxorubicin (DOX), NIR dye IR825 and human histones, which can be used for interventional nucleus-targeted CPT treatment of multidrug resistant tumors by localized delivery of DIR825@histone and laser energy (Fig. 1). Upon localized intervention, DIR825@histone could penetrate tumor tissues via adsorption-mediated transcytosis (AMT), efficiently enter tumor cells and target the cell nucleus. Additionally, DIR825@histone exhibited good photothermal properties and thermally triggered drug release, which are favorable for targeting the CPT effect at the nuclei of tumor cells upon laser irradiation. We show that DIR825@histone through a nucleus-targeted CPT strategy, especially in combination with an interventional NIR laser that facilitated adequate delivery of laser energy inside the tumor, effectively suppressed the growth of multidrug resistant tumors and yielded great survival benefits.

2. Results and discussion

2.1. Preparation and characterization of NPs

Histones were extracted from MCF-7 human breast cancer cells, and the components of H1, H2A, H2B, H3 and H4 were identified by gel electrophoresis (Fig. 2a). DIR825@histone was prepared by fabricating IR825-conjugated histone NPs (IR825@histone) followed by loading DOX inside IR825@histone. A one-step method was used to prepare IR825@histone by conjugating IR825 to histones in anhydrous DMSO followed by self-assembly in aqueous solution. Using SDS-PAGE, we found that the band of the histone-IR825 conjugate could be observed by the naked eye due to the green color of IR825, indicating the successful conjugation of IR825 to histones (Fig. S1). To modulate the size distribution of IR825@histone, the mass ratio of IR825 to histones was set at 1:4, 1:6, 1:8, 1:10 and 1:12. The decreasing mass ratio of IR825 to histones caused a decreasing diameter and an increasing positive surface charge of IR825@histone (Table S1). When the mass ratio of IR825 to

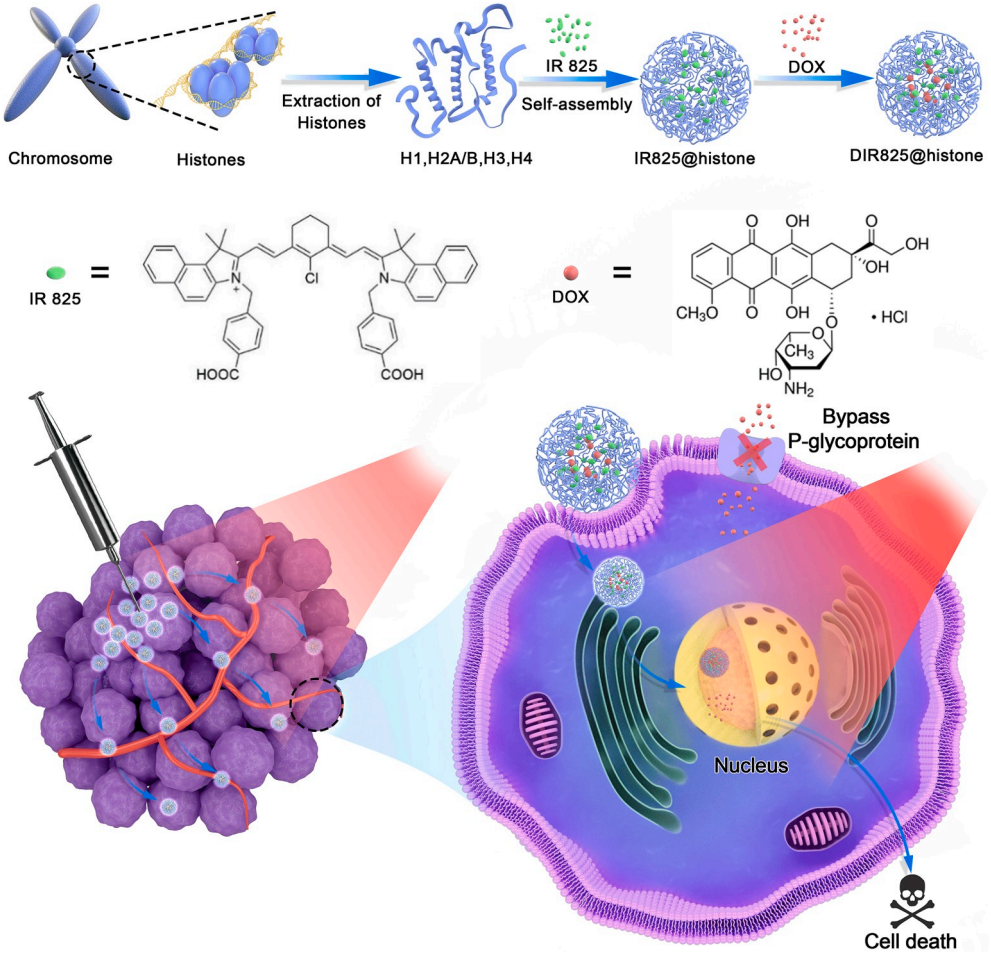

Fig. 1. Schematic illustration shows the preparation process of DIR825@histone and the function of DIR825@histone for interventional nucleus-targeted chemo-photothermal therapy of drug-resistant tumors.

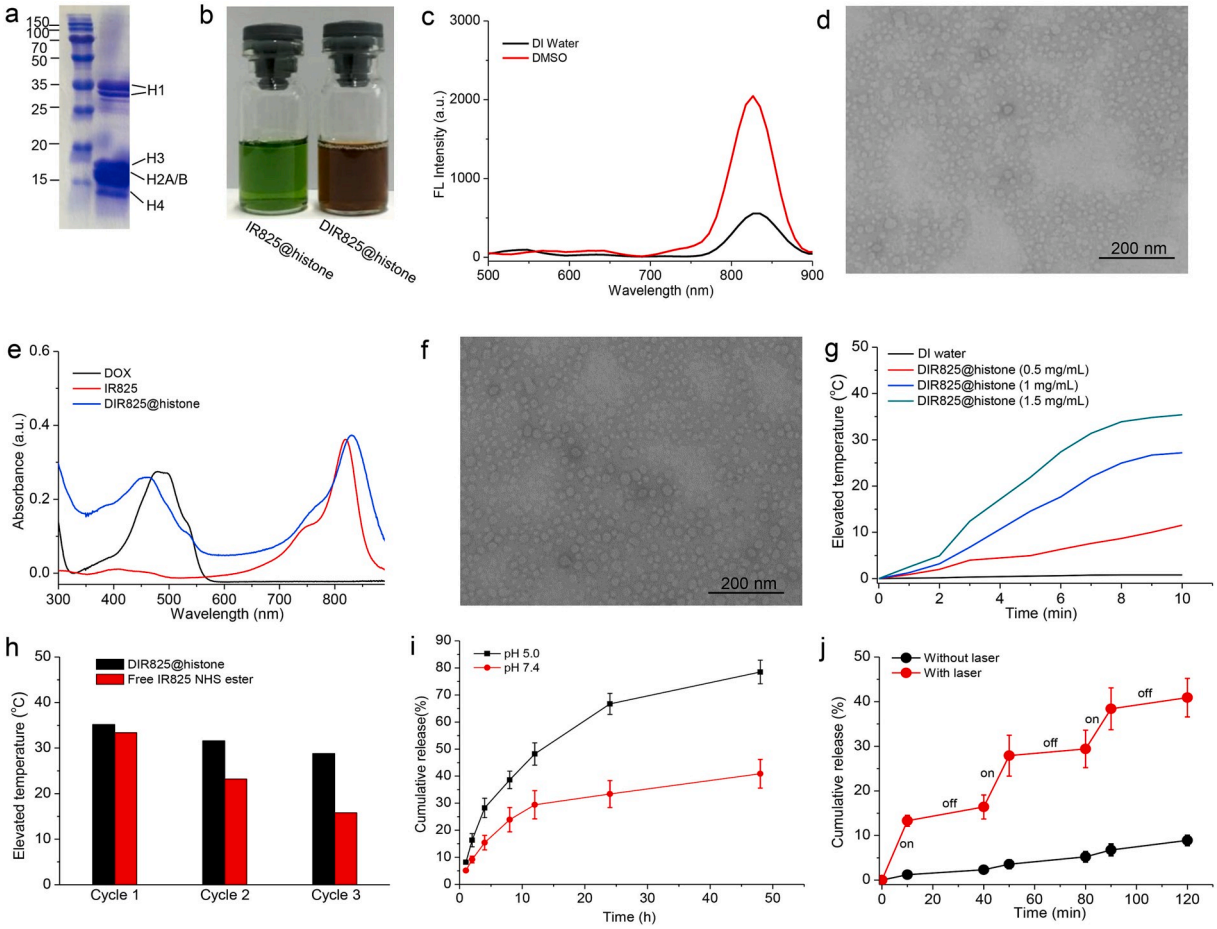

Fig. 2. (a) Identification of the extracted histones by SDS-PAGE. (b) Images of IR825@histone and DIR825@histone suspended in DI water. (c) Fluorescence intensities of IR825@histone in DMSO and DI water. (d) TEM image of IR825@histone. (e) Absorption spectra of DOX, IR825 and DIR825@histone. (f) TEM image of DIR825@histone. (g) Temperature elevations of DIR825@histone under laser irradiation (1 W, 10 min). (h) Temperature elevations of IR825 NHS ester and DIR825@histone at an IR825 concentration of 0.15 mg/mL over three cycles of laser irradiation (10 min, 1 W). (i) DOX release from DIR825@histone at 37 °C in two mediums with pH 7.4 and 5.0, respectively. (j) DOX release from DIR825@histone with three cycles of laser irradiation (10 min of laser on (1 W) and 30 min of laser off).

histones was 1:10 and 1:12, IR825@histone with a diameter of approximately 36 nm was obtained, and this particle size was favorable for passing through the nuclear pore complex (NPC). IR825@histone fabricated at a mass ratio (IR825: histones) of 1:10 was used for the following study due to the satisfactory diameter and loading content of IR825 (9.5 wt%). The chosen IR825@histone was well dispersed (Fig. 2b), and notable fluorescence quenching occurred owing to the aggregation of IR825 inside IR825@histone (Fig. 2c). Transmission electron microscopy (TEM) imaging showed that the chosen IR825@histone had a small size of approximately 30 nm (Fig. 2d). IR825 was firmly anchored in IR825@histone, and no release of IR825 or destruction of NPs was observed by incubating IR825@histone in simulated body fluid at 37 °C for 72 h (Fig. S2 and S3). Doxorubicin hydrochloride (DOX·HCl) could be hydrophobized and encapsulated into IR825@histone to form DIR825@histone in the presence of trimethylamine. With increasing the mass ratio of DOX·HCl to IR825@histone, the loading content of DOX slightly increased and the encapsulation efficiency of DOX decreased (Table S2). DIR825@histone fabricated at a mass ratio (DOX·HCl to IR825@histone) of 1:10 was used for further characterization and following study. The chosen DIR825@histone was well dispersed (Fig. 2b) and showed specific absorptions of IR825 and DOX (Fig. 2e). The properties of DIR825@histone, including the morphology, diameter, zeta potential and colloidal stability, were all similar to those of IR825@histone (Fig. 2f; Fig. S3–S5). All these results demonstrate the successful construction of DIR825@histone and its stability and potential for cell nucleus-targeted drug delivery.

2.2. Photothermal and drug release properties

Aqueous dispersions of DIR825@histone exhibited significantly elevated temperatures upon laser irradiation. The temperature elevation amplitude increased obviously with increasing NP concentration and laser power (Fig. 2g; Fig. S6). IR825 immobilized in DIR825@histone exhibited well-repeated temperature elevation (Fig. 2h) and improved photostability (Fig. S7) compared with the free water-soluble IR825 derivative (IR-825 NHS ester) when treated with three cycles of laser irradiation. This phenomenon can be attributed to the protective effect of nanovesicles on the photostability of NIR dyes [33]. The passive DOX release pattern from DIR825@histone was studied in two mediums with pH 7.4 and 5.0, respectively. As shown in Fig. 2i, the passive DOX release rates from DIR825@histone were both time and pH-dependent. Specifically, the passive DOX release rates increased as the pH values of the release media decreased (from approximately 41.2% at pH 7.4 to approximately 78.6% at pH 5.0 within 48 h). The accelerated DOX release from DIR825@histone at pH 5.0 was likely attributed to the rapid protonization of the hydrophobic DOX in acidic conditions. Next, the laser-triggered drug release was studied by repeatedly irradiating DIR825@histone with a 10-min laser-on period (1 W) followed by a 30-min laser-off period. As exhibited in Fig. 2j, rapid DOX release was

observed during the laser-on period, and slowed release was observed when the laser was switched off. After three laser on/off cycles within 120 min, the cumulative drug release was 40.8%, which is much faster than passive drug release. The accelerated DOX release upon laser irradiation was likely attributed to the significantly elevated temperature throughout DIR825@histone, which enhances the dissolution of DOX and accelerate the exchange rate between the internal space of the NPs and external solution environment [34]. Moreover, the DOX release amplitude could be increased by increasing the output power of the laser cycles (Fig. S8). These characteristics are advantageous for DIR825@histone to achieve efficient and controllable intranuclear synergistic CPT treatment after localized tumor intervention, although it may take time for DIR825@histone to penetrate the tumor and to be internalized by cancer cells.

2.3. Intracellular and intranuclear accumulation of NPs

The DOX-resistant MCF-7 cell line (MCF-7/ADR, overexpression of P-gp) was used to investigate the intracellular uptake and intranuclear accumulation of DIR825@histone. Free DOX and DIR825@HSA (made by DOX, IR825 and human serum albumin (HSA)) were used for comparison. The prepared DIR825@HSA had similar colloidal stability, morphology, size, drug loading contents (9.9 wt% for IR825, 5.4 wt% for DOX) and drug release profile (pH-dependent and photothermal-triggered drug release) to DIR825@histone but possessed a negative surface charge (Fig. S9, S10, S13 and S14). At an equal incubating concentration of DOX (5 μg/mL), free DOX showed limited and nearly unchanged uptake by MCF-7/ADR cells from 2 h to 8 h post-incubation due to P-gp-mediated drug efflux, whereas the intracellular DOX amount in the DIR825@HSA- and DIR825@histone-treated cells notably increased over time (Fig. 3a and b). After 8 h of incubation, the fluorescence intensity and the content of DOX in DIR825@histone-treated cells were increased 1.9- and 2.2-fold compared with that in DIR825@HSA-treated cells, respectively, indicating that DIR825@histone is more likely to be taken up by cells than DIR825@HSA.

The intracellular locations of the two NPs were visualized by confocal laser scanning microscopy (CLSM). For both DIR825@HSA and DIR825@histone, increased intracellular uptake could be observed with time; However, DIR825@HSA was mainly located in the cytoplasm, whereas DIR825@histone showed significantly increased intranuclear accumulation over time (Fig. 3c).

By detecting the intracellular amounts of DOX and IR825, we found that DIR825@HSA exhibited lower intracellular uptake than DIR825@histone at all incubation time points (Fig. 3d). After 8 h of

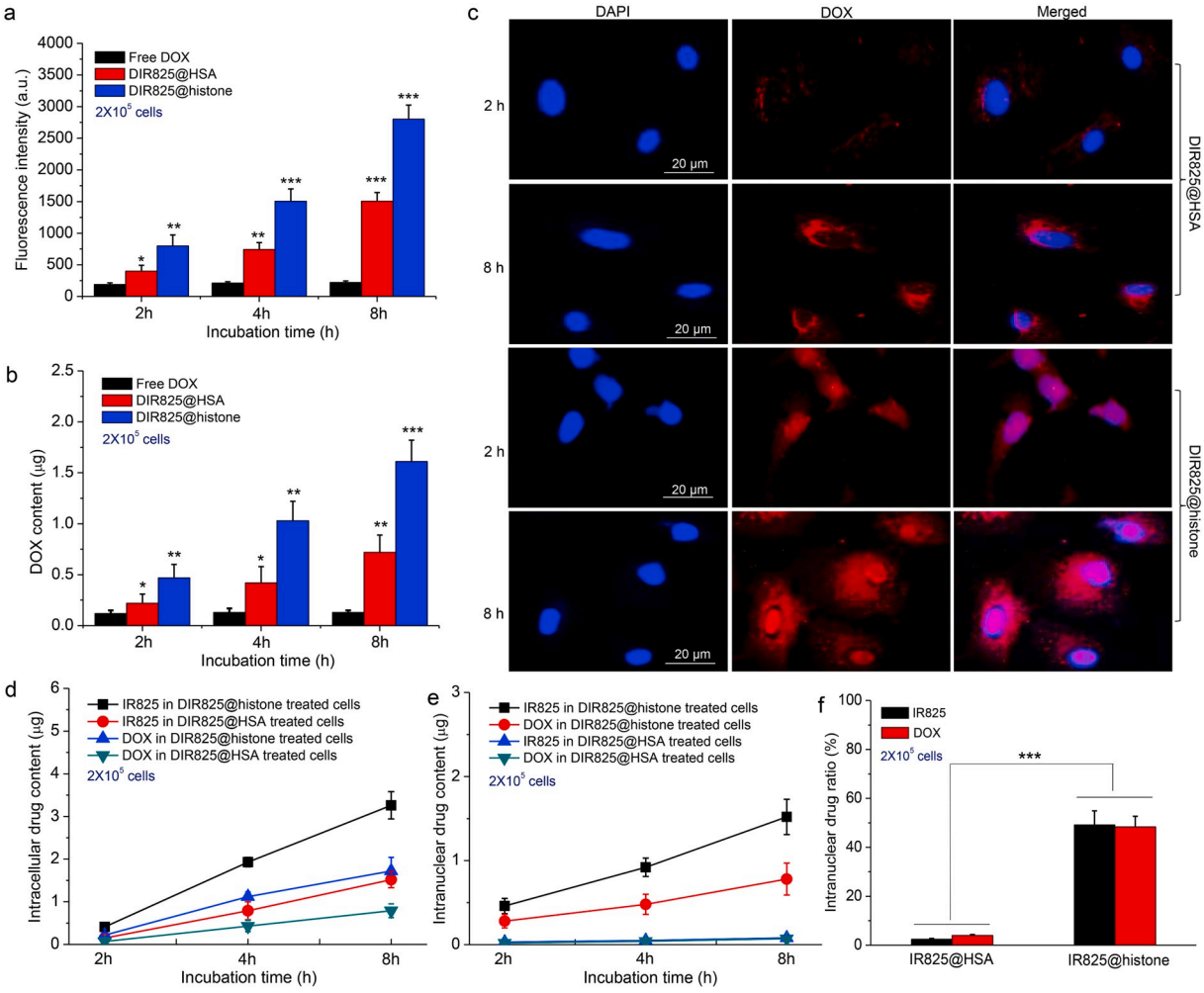

Fig. 3. (a) Fluorescence intensities and (b) contents of DOX in MCF-7/ADR cells incubated with free DOX, DIR825@HSA and DIR825@histone at equal incubation concentrations of DOX (5 μg/mL). (c) CLSM images of MCF-7/ADR cells incubated with DIR825@HSA and DIR825@histone at equal amounts of DOX (5 μg/mL). (d) DOX and IR825 contents in MCF-7/ADR cells treated with DIR825@HSA and DIR825@histone. (e) DOX and IR825 contents in the nucleus of MCF-7/ADR cells treated with DIR825@HSA and DIR825@histone. (f) Intranuclear ratios of DOX and IR825 in MCF-7/ADR cells at 8 h post-incubation with DIR825@HSA and DIR825@histone. For (d), (e) and (f), DIR825@HSA and DIR825@histone were used at an equal dosage of DOX (5 μg/mL), for which the IR825 dosage for the DIR825@HSA group was 1.1-fold that of the DIR825@histone group. *, $P < 0.05$; **, $P < 0.01$; ***, $P < 0.001$.

incubation, the intranuclear amounts of DOX and IR825 in DIR825@histone-treated cells were increased approximately 11- and 19-fold compared with that in DIR825@HSA-treated cells, up to 48.4% and 49.2% of the total intracellular amounts of DOX and IR825, respectively (Fig. 3e and f). Our results indicated that DIR825@histone is more likely to be internalized by resistant cancer cells and then easily passes through the NPC for intranuclear delivery of DOX and IR825.

2.4. In vitro therapeutic potentials

MCF-7 and MCF-7/ADR cells were used to evaluate the in vitro chemotherapeutic efficiency of DIR825@histone compared with DIR825@HSA and free DOX. All free DOX and the two NPs showed chemo-cytotoxicity to the test cells (Fig. 4a). Due to DOX resistance, the IC50 of free DOX against MCF-7/ADR cells was 154.7 ± 11.26 μg/mL, which was increased approximately 14-fold compared with MCF-7 cells (11.68 ± 1.21 μg/mL). Both DIR825@histone and DIR825@HSA showed improved chemo-cytotoxicity compared with free DOX. The IC50 values of DIR825@HSA against MCF-7 and MCF-7/ADR cells were 5.68 ± 0.31 and 10.89 ± 0.79 μg/mL, respectively. The IC50 values of DIR825@histone against MCF-7 and MCF-7/ADR cells were 1.98 ± 0.15 and 2.69 ± 0.26 μg/mL, respectively. The improved chemotherapeutic cytotoxicity of DIR825@HSA against MCF-7 and MCF-7/ADR cells was likely attributed to its accelerated DOX release in acidic environment (Fig. S14a), by which accelerated DOX release can be achieved in acidic endosomes when internalized by cancer cells. Comparatively, DIR825@histone exhibited significantly greater chemo-cytotoxicity than DIR825@HSA due to nucleus-targeted drug delivery. Notably, the IC50 of DIR825@histone against MCF-7/ADR cells was only increased 1.3-fold compared with MCF-7 cells, suggesting sufficient DOX anticancer activity in MDR cells.

Drug-free IR825@histone was used to study the influence of the nucleus-targeted PTT effect on the viability and drug resistance of MDR cells, and negatively charged IR825@HSA with a similar size to IR825@histone was used for comparison (Fig. S11 and 12). As shown in Fig. 4b, at all IR825 concentrations, IR825@histone displayed greater inhibition rates against MCF-7/ADR cells than IR825@HSA at 24 h post laser treatment (1 W/cm^2, 10 min). At an IR825 concentration of 4 μg/mL (the concentration of IR825@histone was approximately 40 μg/mL), the inhibition rate of IR825@histone against MCF-7/ADR cells upon laser irradiation was nearly approximately 86%, representing an approximately 2-fold increase compared with that of IR825@HSA, and

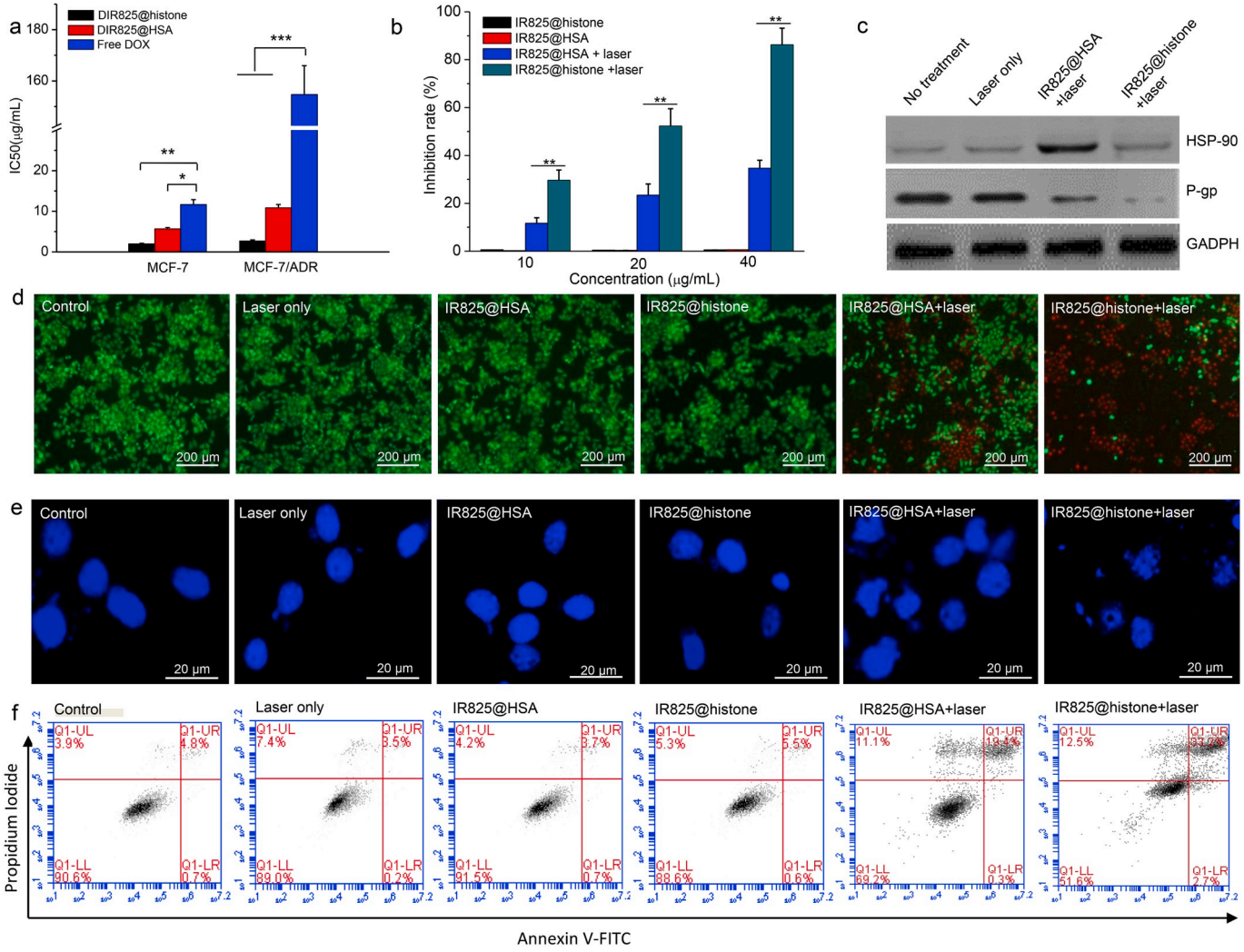

Fig. 4. (a) IC50 values of free DOX, DIR825@HSA and DIR825@histone against MCF-7 and MCF-7 cells after 24 h of treatment. (b) The inhibition rates of IR825@histone and IR825@HSA against MCF-7/ADR cells at different IR825 concentrations with or without laser irradiation (1 W/cm^2, 10 min). (c) Analysis of the P-gp and HSP-90 levels in MCF-7/ADR cells at 6 h after different treatments. Laser irradiation: 1 W/cm^2, 10 min; the IR825 concentration was 40 μg/mL. (d) Calcein-AM/PI staining of MCF-7/ADR cells at 24 h after different treatments and (e) nuclear morphologies of MCF-7/ADR cells at 6 h after different treatments (red signal, dead cells; green signal, live cells; blue signal, nucleus). Laser irradiation: 1 W/cm^2, 10 min; the IR825 concentration was 40 μg/mL. (f) Apoptosis assay of MCF-7/ADR cells at 24 h after different treatments. Laser irradiation: 1 W/cm^2, 10 min; the IR825 concentration was 4 μg/mL *, $P < 0.05$; **, $P < 0.01$; ***, $P < 0.001$.

Calcein-AM/PI double staining and flow cytometry test confirmed similar results (Fig. 4d and f). In addition, IR825@histone with laser treatment remarkably inhibited the expression of P-gp and the HSP-90 response in MCF-7/ADR cells (Fig. 4c; Fig. S15) and destroyed the cell nucleus compared with IR825@HSA (Fig. 4e). This result suggested that, compared with the PTT effect in the cytoplasm, targeting the PPT effect to the nuclei of MDR cells significantly improved the cancer cell killing effect, promoted intracellular MDR reversion and reduced the heat shock response, which generally protects tumor cells from cell death due to hyperthermia [35]. The synergistic CPT treatment mediated by DIR825@histone and NIR laser irradiation increased the inhibition rate of MCF-7/ADR cells compared with chemotherapy mediated by DIR825@histone and PTT treatment mediated by IR825@histone and NIR laser irradiation (Fig. S16), and the therapeutic outcome depended on the drug dosage, laser power and irradiation period (Fig. S16 and Table S3). As shown in Table S3, DIR825@histone at a dose of 10 μg/mL exhibited approximately the same inhibition efficiency against MCF-7 and MCF-7/ADR cells at a laser power of 2 W/cm^2 and an irradiation period of 10 min. These results indicated that DIR825@histone-mediated nucleus-targeted CPT treatment significantly increased the efficiency of cell killing and potentially overcame the intracellular resistance to DOX.

2.5. Transcytosis and tumor penetration of NPs

Cationic NPs can penetrate multiple cell layers by inducing adsorption-mediated transcytosis (AMT) [36]. Here, both in vitro and in vivo studies were used to assay the transcytosis behavior and tumor penetration performance of the cationic DIR825@histone. For comparison, DIR825@HSA with a negative surface charge was also investigated.

A transwell insert method, as illustrated in Fig. 5a, was used to investigate the transcytosis behavior of the two NPs in vitro. As shown in Fig. 5b, after 3 h of incubation, 46.9% of DIR825@histone penetrated the cell layer from the apical chamber to the basolateral chamber, and this ratio was remarkably increased compared with that of DIR825@HSA (3.6%). This high cell penetration performance of DIR825@histone can be attributed to its cationic surface. Transcytosis is an energy-dependent process consisting of cellular uptake on one side and exocytosis on the other side [36,37]. As shown in Fig. 5c, low

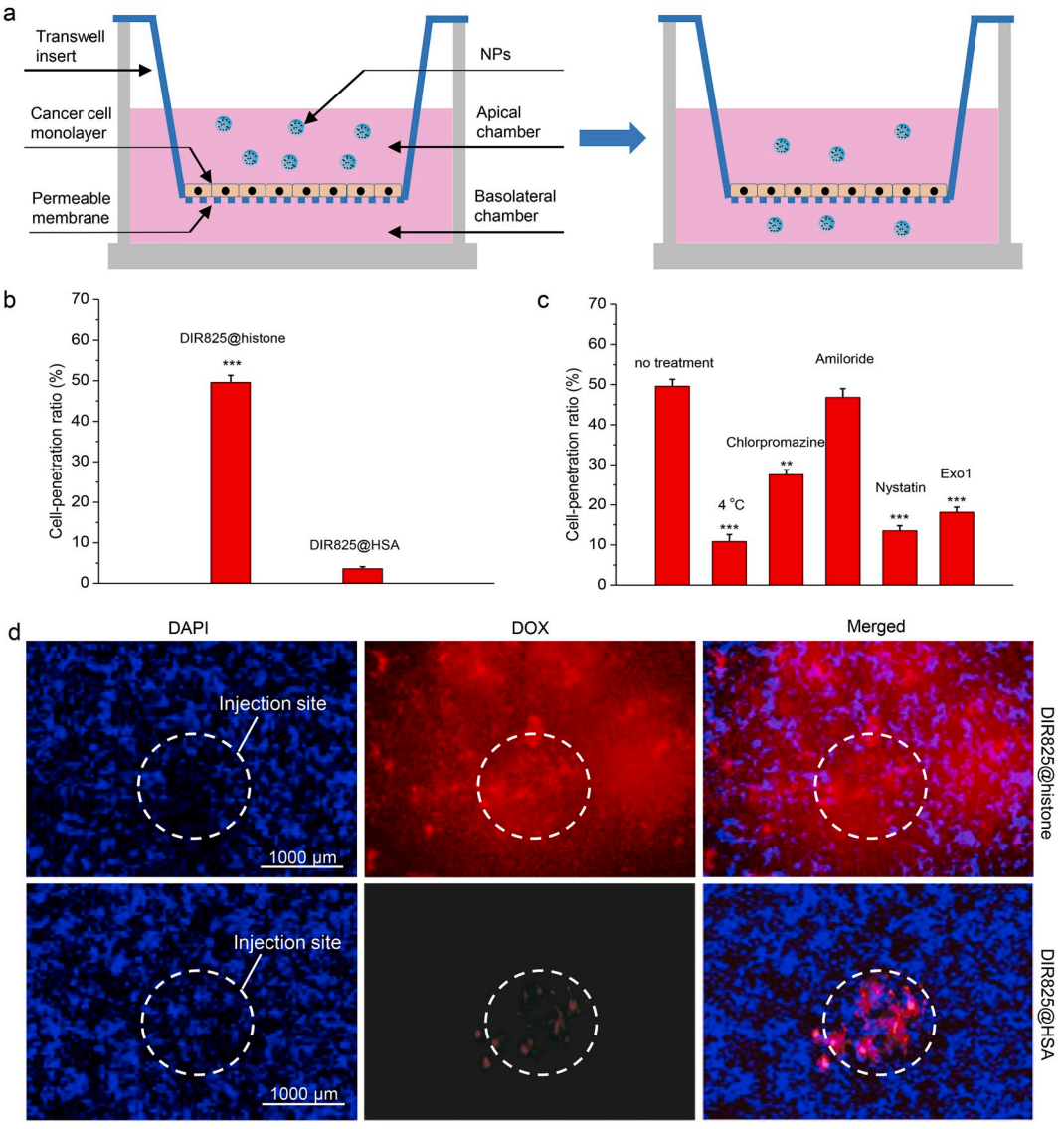

Fig. 5. (a) Illustration of the transwell insert method for investigating the transcytosis behavior of NPs. (b) The ratios of DIR825@histone and DIR825@HSA that penetrated across the cell layer from the apical chamber to the basolateral chamber over 3 h. (c) The effects of low temperature and several inhibitors on the cell-layer penetration of DIR825@histone. (d) The tumor penetration performance of DIR825@histone and DIR825@HSA at 3 h after tumor penetration. *, $P < 0.05$; **, $P < 0.01$; ***, $P < 0.001$.

temperature (4 °C), chlorproma-zine (clathrin-mediated endocytosis inhibitor), nystatin (caveolae-endocytosis inhibitor) and Exo1 (exocytosis inhibitor) significantly decreased the cell penetration ratio of DIR825@histone. These results indicated that the cell penetration process of DIR825@histone is energy dependent and relies on clathrin- and caveolae-mediated endocytosis and exocytosis, which is consistent with the characteristics of AMT. We further established xenograft tumors in mice to evaluate the tumor penetration performance of DIR825@histone. As expected, DIR825@histone exhibited greater tumor tissue permeability than DIR825@HSA in grafted MCF-7/ADR tumors after localized intervention (Fig. 5d). In addition, DIR825@histone could be efficiently internalized by tumor cells and accumulated in the nucleus when penetrating tumor tissues (Fig. S17).

2.6. Antitumor efficacy in vivo

To evaluate the interventional chemotherapeutic efficiency of DIR825@histone, tumor-bearing mice were administered DIR825@histone, DIR825@HSA or free DOX by multipoint intratumor injections at an equal DOX dosage of 10 mg/kg (Fig. 6a). As shown in Fig. 6b, free DOX exerted no inhibitory effect on MCF-7/ADR tumors, whereas DIR825@histone and DIR825@HSA inhibited MCF-7/ADR tumor growth. Compared with DIR825@HSA, DIR825@histone achieved improved chemotherapy outcomes against MCF-7/ADR tumors, which was likely attributed to its efficient tumor-penetrating and nucleus-targeting abilities. CPT treatment was performed by irradiating the tumors with a laser (0.5 W, 10 min) at 6 h after the multipoint intratumor injection of DIR825@histone or DIR825@HSA. DIR825@histone and DIR825@HSA were administered at an equal DOX dosage of 10 mg/kg, for which the IR825 dosage for the DIR825@HSA group was increased approximately 1.1-fold compared with the DIR825@histone group. Laser irradiation was implemented both extracorporeally and interventionally (Fig. 6a). The laser devices were used as shown in Fig. S18. For extracorporeal laser irradiation, the tumor was covered with a laser beam from an extracorporeal optical fiber. For interventional laser irradiation, the laser beam was delivered inside the tumor by a puncture laser fiber. Without the administration of NPs, both extracorporeal and interventional laser irradiation cannot heat tumor tissue and induce the apoptosis of tumor cells (Fig. 6d and g). Compared with the extracorporeal laser, the interventional laser could better heat tumors from the inside to the edge and reduce skin injury at the same output power in the presence of DIR825@histone (Fig. 6d, e and 6f). For DIR825@histone and DIR825@HSA, CPT treatment increasingly inhibited tumor growth compared with chemotherapy alone (Fig. 6b and c). In addition, the

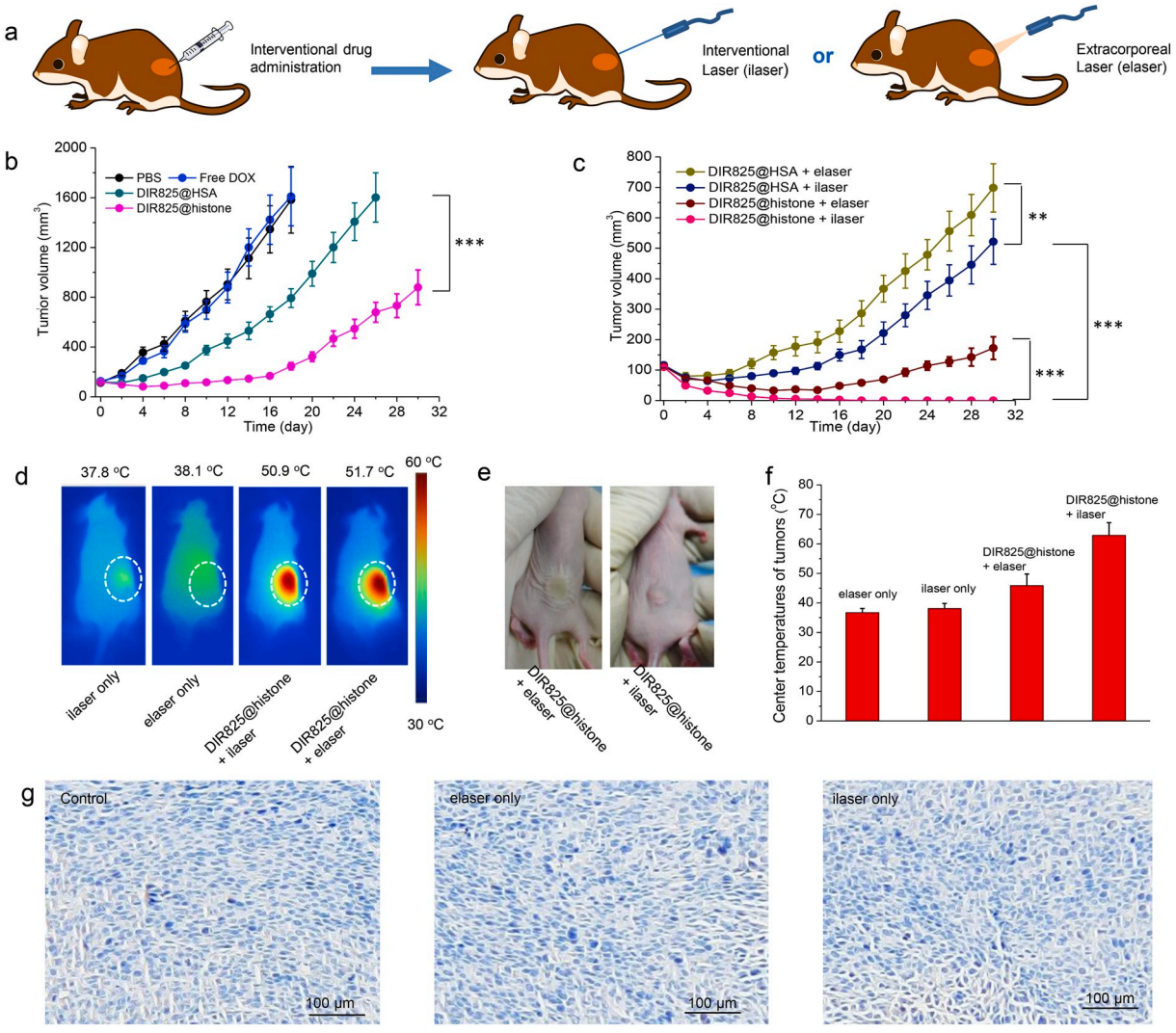

Fig. 6. (a) Illustration of the method used to investigate the antitumor efficiency of NPs in vivo. (b), (c) The tumor growth curves of mice in different treatment groups. (d) Surface temperatures of tumors in mice with different treatments. (e) Representative images of skin covering the tumor treated with DIR825@histone + ilaser and DIR825@histone + elaser. (f) Center temperatures of tumors in mice with different treatments. (g) Representative tumor sections incubated with caspase-3 antibody. *, $P < 0.05$; **, $P < 0.01$; ***, $P < 0.001$.

interventional laser led to improved CPT outcomes compared with the extracorporeal laser (Figs. 6c and 7). With two laser modalities, DIR820@histone produced greater therapeutic outcomes than DIR820@HSA. Notably, DIR820@histone + interventional laser resulted in the best therapeutic outcomes; the tumors shrank gradually and finally disappeared, no recurrence occurred until 30 days after treatment. We found that DIR820@histone + interventional laser could more effectively downregulate the expression of P-gp (for drug efflux), VEGF (relevant to tumor growth and angiogenesis), MMP2 and MMP9 (relevant to tumor invasion) in the tumor compared with other treatments (Fig. 8a). Further study showed that, over 60 days posttreatment, 80% of the mice treated with DIR820@histone + interventional laser were alive, and the median survival time was significantly prolonged compared with that of the other treatment groups (Fig. 8b).

Toxicological assessments were performed during treatment. Compared with the PBS group, mice in the other treatment groups showed no apparent body weight loss or histological damage in the main organs (Fig. 8c; Fig S19). In several treatment groups, hematological parameters, including white blood cell (WBC), platelet (PLT) and granulocyte (GRN) counts increased to different degrees at 1 day

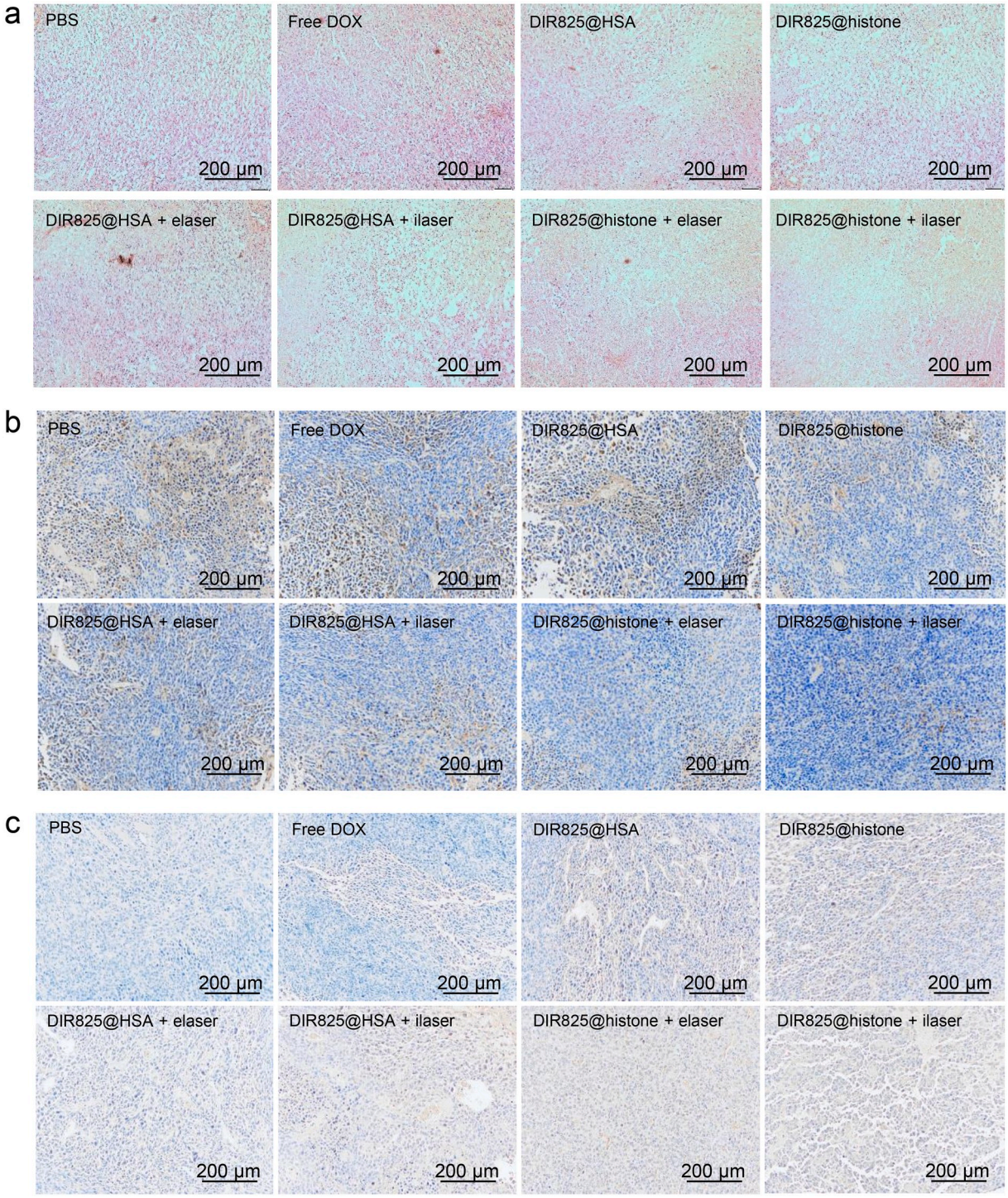

Fig. 7. The tumor sections at 1 day after different treatments. (a) Tumor sections with H&E staining. (b) Ki-67 antibody and (c) caspase-3 antibody incubated tumor sections.

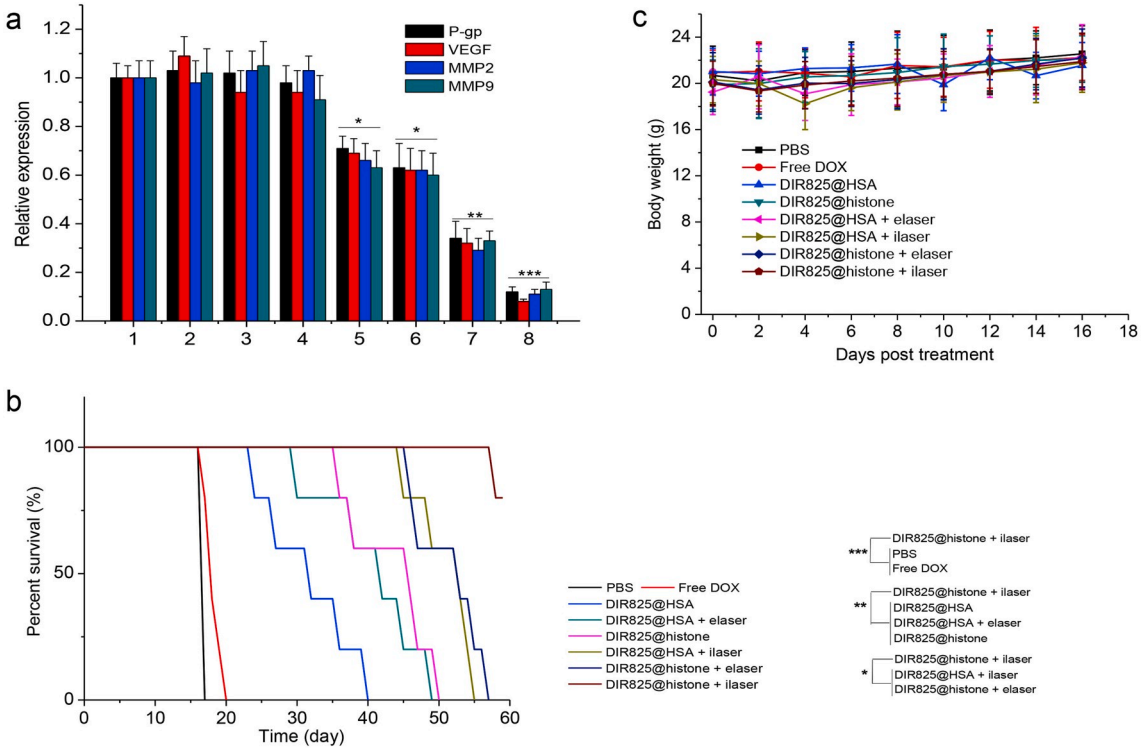

Fig. 8. (a) The expression levels of P-gp, VEGF, MMP2 and MMP9 in tumor tissues at 1 day after different treatments. (1) PBS; (2) Free DOX; (3) DIR825@HSA; (4) DIR825@histone; (5) DIR825@HSA + elaser; (6) DIR825@HSA + ilaser; (7) DIR825@histone + elaser; (8) DIR825@histone + ilaser. (b) The percent survival of mice in different groups monitored over 60 days after different treatments. (c) Variation in the body weight of tumor-bearing mice over 16 days after different treatments. *, $P < 0.05$; **, $P < 0.01$; ***, $P < 0.001$.

posttreatment due to treatment-induced tumor inflammation, and these fluctuating parameters were almost within the normal range at 16 days post-treatment (Table S4 and S5). AST, ALT, ALP, BUN and CRE serum levels in the mice in the treatment groups showed no apparent change compared with those in the PBS group at 1 day and 16 days posttreatment (Table S6 and S7), suggesting the undamaged functions of the liver and kidney.

3. Conclusions

In summary, we successfully designed a drug nanococktail of DIR825@histone for interventional nucleus-targeted CPT of multidrug resistant tumors by locally delivering DIR825@histone and using an NIR laser. DIR825@histone exhibited tailored properties for interventional nucleus-targeted CPT treatment, including satisfactory tumor-penetration and nucleus-targeting efficiencies, high photostability and light-controlled drug release. By targeting the nucleus, DIR820@histone showed greater PPT outcomes, including direct destruction of the cell nucleus and more significant downregulation of P-gp and HSP-90. In vivo studies showed that nucleus-targeted CPT mediated by DIR820@-histone not only effectively kills MDR cells but also remarkably down-regulates genes related to tumor progression. An interventional laser can better assist DIR825@histone in inhibiting multidrug resistant tumor growth and progression by sufficiently heating the tumor tissue. Thus, DIR820@histone and its mediated interventional nucleus-targeted CPT strategy may hold great promise for treating multidrug resistant tumors. It should be pointed out that, for interventional therapy using nano-medicine, image guidance is very important to monitor the dynamic tumor distribution of nanomedicine in practical, which is favorable for choosing the optimal treatment opportunity. Therefore, medical imaging functions with high spatial resolution should be integrated with DIR825@histone to construct a theranostic nanococktail, which is worth investigating in the future.

4. Materials and methods

4.1. Materials

Human serum albumin (HSA); 1-ethyl-3-(3-dimethylaminopropyl) carbodiimide (EDC); N-hydroxy-succinimide (NHS); 3-(4,5-dimethylthiazol-2-yl)-2,5-diphenyltetrazolium bromide (MTT); doxorubicin hydrochloride (DOX·HCl); propidium iodide (PI); calcein acetoxymethyl ester (calcein-AM) and 4′6-diamidino-2-phenylindole (DAPI) were purchased from Sigma-Aldrich. IR-825 and IR-825 NHS ester were purchased from Xi'an Ruixi Biological Technology Co., Ltd. All other chemicals and reagents were of analytical grade. Deionized (DI) water (18.2 MΩ cm) was obtained from a Milli-Q purification system.

4.2. Extraction of histones

Histone extraction was performed as described previously [38]. In brief, 1×10^7 cells were washed with ice-cold PBS and lysed in extraction buffer containing 0.2% NP40 and complete protease inhibitors on ice for 10 min. After centrifugation at 6500 g for 5 min, the precipitate was harvest and washed with extraction solution (without NP40) followed by incubating on ice for 1 min to obtain cell nuclei. Cell nuclei were lysed using a no-salt buffer and vortexed. After incubating at 4 °C for 30 min, the sample was centrifuged at 6500 g for 5 min, and the precipitate was suspended in 400 μL of high-salt buffer and incubated at 4 °C for 30 min. After centrifugation at 4 °C for 10 min (16,000 g), the supernatant was harvested and dialyzed with 100–200 mM NaCl. Then, the sample was recentrifuged at 16,000 g for 10 min to separate supernatant containing histones. Purified histones was obtained by dialyzing the histones contained supernatant with DI water followed by freeze-drying.

4.3. Fabrication of the nanoparticles

IR825 was reacted with EDC and NHS at a molar ratio of 1:1:1 in 1 mL of anhydrous DMSO for 1 h. Subsequently, the mixture was continuously added into 1 mL of anhydrous DMSO containing 100 mg of histones while stirring. After 24 h of reaction, 10 mL of DI water was continuously added to the reaction solution. Then, IR825@histone was purified using a 100-kDa filter (Millipore). For drug loading, 20 mg of IR825@histone and different amount of DOX·HCl were mixed in 4 mL DI water, at the mass ratio of 2:1, 5:1, 10:1, 15:1, 20:1, respectively. Then, trimethylamine (twice the molar amount of DOX·HCl) was slowly added. After 24 h of incubation, DIR825@histone was purified by repeated rinsing with pH 7.4 PBS buffer using a 100-kDa filter. IR825@HSA and DOX-loaded IR825@HSA (DIR825@HSA) were fabricated using the same method for IR825@histone and DIR825@histone by replacing histones with HSA.

4.4. Characterization of the nanoparticles

The morphologies of the NPs were observed using a transmission electron microscope (TEM, JEM-2100). The size distributions and zeta potentials of the NPs were evaluated using a 90Plus/BI-MAS instrument (Brookhaven Instruments Co., U.S.A.). UV/Vis absorption spectra were measured using a Varian 4000 UV–Vis spectrophotometer. The loading contents of DOX and IR825 were evaluated by dissolution of the NPs in DMSO and measuring the fluorescence intensities using a LUMINA fluorescence spectrophotometer (Thermo Scientific).

4.5. Photothermal investigation

Briefly, 3.0 mL of DIR825@histone aqueous solution at 0.5, 1 and 1.5 mg/mL was added to a quartz cuvette and irradiated using an 808 nm continuous-wave NIR laser (STONE Laser, China). In addition, 3.0 mL of DIR825@histone aqueous solution at 0.5 mg/mL was added to a quartz cuvette and irradiated using an 808 nm continuous-wave NIR laser at different output powers. The temperature increase was recorded with a digital thermometer.

4.6. Drug release

DIR825@histone was suspended in several tubes containing pH 7.4 PBS buffer or pH 5.0 PBS buffer. Then, the tubes were placed at 37 °C under moderate shaking. At different time points, the NP solution was filtered via centrifugation using a 100-kDa filter, and the DOX content in the filtrate was evaluated. To study drug release with laser irradiation, DIR825@histone was suspended in several tubes containing pH 7.4 PBS buffer. Then, the NP solutions were treated with three laser on/off cycles (1 W laser on for 10 min, followed by laser off for 30 min). Afterwards, the NP solution was filtered via centrifugation using a 100-kDa filter, and the DOX content in the filtrate was evaluated. The DOX content was measured using a LUMINA fluorescence spectrophotometer through a standard curve method.

4.7. Cell lines and animal models

MCF-7 and its DOX-resistant cell line MCF-7/ADR were cultured in Dulbecco's modified Eagle's medium (DMEM) (HyClone, Thermo Scientific) containing 10% fetal bovine serum (FBS) at 37 °C with 5% CO_2. Female BALB/c nude mice obtained from Beijing Vital River Laboratories were used to establish a tumor model. Tumors were generated by injection of 5×10^5 cells into the back of each mouse. All animal procedures were approved by the Animal Care and Use Committee of Northeast Forestry University, performed in accordance with the NIH guidelines, and carried out ethically and humanely.

4.8. Intracellular and intranuclear drug delivery

MCF-7/ADR cells were incubated with free DOX, DIR825@histone and DIR825@HSA for different time periods. Confocal laser scanning microscopy (CLSM) was used to observe the intracellular locations of the two NPs through the fluorescent signal of DOX. The cells were fixed with 4% paraformaldehyde, treated with 10% Triton X-100 and stained with DAPI. To quantify the intracellular uptake of the NPs, the incubated cells were dissolved in DMSO for 12 h in the dark. Then, the amounts of DOX and IR825 were measured. To quantify the intranuclear accumulation of NPs, the nuclei were isolated from the incubated cells using a detergent-free nuclei isolation kit (Minute). The isolated cell nuclei were dissolved in DMSO for 12 h in the dark, and the amounts of DOX and IR825 were measured by a LUMINA fluorescence spectrophotometer (Thermo Scientific).

4.9. In vitro cytotoxicity assay

MCF-7 and MCF-7/ADR cells were incubated with DIR825@histone, DIR825@HSA and free DOX at different DOX concentrations. After 24 h of incubation, the IC50 values of DIR825@histone, DIR825@HSA and free DOX against the test cells were assayed. To investigate the photothermal cytotoxicity, MCF-7/ADR cells were incubated with drug-free IR825@histone and IR825@HSA at different IR825 concentrations. After 8 h of incubation, the cells were exposed to NIR laser. After 24 h of laser irradiation, cell viability was assayed using the MTT method. To observe cell viability, calcein-AM, PI and DAPI were used to stain viable cells, dead cells and cell nuclei, respectively. To investigate chemo-photothermal cytotoxicity, MCF-7/ADR cells were incubated with DIR825@histone and DIR825@HSA. After 8 h of incubation, the cells were irradiated by NIR laser. After laser irradiation, the cell viability was measured by calcein-AM/PI double staining and the MTT method.

4.10. Cell apoptosis analysis

After different treatments, MCF-7/ADR cells were trypsinized, washed with PBS and harvested by centrifugation at 3000 rpm. Then, cells were resuspended in 500 μL binding buffer and stained with Annexin V-FITC and PI according to the protocol (SC123-01, Seven). After the incubation in the dark at room temperature for 20 min, the percentage of apoptotic cells were assessed by flow cytometry.

4.11. Transcytosis and tumor penetration assay

Transwell inserts (Greiner Bio-One) with a 33.6-mm^2 surface area and a 3-μm pore size were placed on a 24-well plate and covered with MCF-7/ADR cells. Each well was filled with 100 mM HEPES buffer (pH 7.4). Then, NP suspensions were added to the apical chambers, and the penetration ratio of the NPs was calculated according to the following formula: amount of NPs in the basolateral chamber/total amount of NPs × 100%. Low-temperature treatment and inhibitors (including chlorpromazine, nystatin, amiloride and Exo1) for endocytosis and exocytosis were used to understand the transcytosis mechanism of DIR825@histone. For in vivo evaluation, NPs were locally injected into the grafted MCF-7/ADR tumors in mice. The tumor penetration performance of NPs was observed by cryosections of frozen tumor tissues. DAPI was used to stain the nuclei of tumor cells, and the distribution of NPs in the tumor tissue was visualized based on the fluorescence signal of DOX. To quantify the intracellular uptake of the NPs after intratumor injection, the treated tumor tissues were digested by trypsin (37 °C, 30 min) and tumor cells was extracted, counted and dissolved in DMSO for 12 h in the dark. Then, the amounts of DOX and IR825 were measured. To quantify the intranuclear accumulation of the NPs after intratumor injection, the nuclei were isolated from the tumor cells using a detergent-free nuclei isolation kit (Minute). The isolated cell nuclei were dissolved in DMSO for 12 h in the dark, and the amounts of DOX and IR825 were

measured using a LUMINA fluorescence spectrophotometer (Thermo Scientific).

4.12. In vivo antitumor study

Mice bearing MCF-7/ADR tumors were randomly divided into 8 groups (n = 5) and administered PBS, DOX, DIR825@HSA, DIR825@-histone, DIR825@HSA + elaser, DIR825@HSA + ilaser, DIR825@histone + elaser or DIR825@histone + ilaser. For drug administration, each mouse was intratumorally injected with 20 μL of an aqueous solution of NPs or free drugs. Laser irradiation was applied both extracorporeally and interventionally (808 nm, 0.5 W, 10 min). A thermal imager (PTi120, FLUKE) was used to record the surface temperature of the tumor. A thermometer probe was used to detect the temperature inside the tumor. The body weights of the mice and the tumor sizes were measured during the experimental period. Tumor volume was measured and calculated according to the following formula: tumor volume = (tumor length) × (tumor width)^2/2.

4.13. Gene and protein expression analysis

The western blotting procedure was performed according to our previous study [11]. The antibodies were purchased from BioLegend. Real-time PCR was used to determine gene expression in the tumors. The total RNA of tumor tissue was extracted using TRIzol (Invitrogen, USA). cDNA was synthesized using a high-capacity cDNA Reverse Transcription kit (Invitrogen, USA). Glyceraldehyde 3-phosphate dehydrogenase (GAPDH) was used as an internal control.

4.14. Histology and immunohistochemistry

To assess tissue morphology, hematoxylin and eosin (H&E) staining was performed on paraffin sections using a standard protocol. To determine cell proliferation and apoptosis, tumor tissues were analyzed by immunohistochemistry methods. In brief, paraffin sections were deparaffinized and rehydrated. Then, the tissue sections were placed in sodium citrate buffer (pH = 6) and heated to 95 °C for 4 min followed by incubation with 3% w/v H_2O_2 for 25 min. After blocking with 2% w/v BSA, the sections were incubated with caspase-3 (D120074, Sangon biotech) and Ki-67 antibody (abs 130135, Absin) overnight at 4 °C. Then, the sections were incubated with secondary antibody and diaminobenzidine (DAB) followed by counterstaining with hematoxylin and destained with 1% hydrochloric acid and alcohol. Finally, all the sections were sealed by neutral gum and observed by microscope.

4.15. Toxicology evaluations

For hematology examination, fresh blood samples were collected from mice and directly assayed through a hematology analyzer (HF-3800, Hanfang, China). For blood biochemical examination, serum was collected from fresh blood samples by centrifugation at 4 °C (13,000 rpm for 10 min) and assayed through a semiautomatic biochemistry analyzer (HF–800C, Hanfang, China). The major organs, including the liver, heart, kidney, spleen, and lung, were collected, and analyzed for histopathological changes after hematoxylin/eosin (H&E) staining.

4.16. Statistical analysis

The data in the manuscript were statistically analyzed using Origin 8.0. The results were compared using one-way analysis of variance (ANOVA) (*P < 0.05, **P < 0.01 and ***P < 0.001).

Declaration of competing interest

The authors declare that they have no known competing financial interests or personal relationships that could have appeared to influence the work reported in this paper.

CRediT authorship contribution statement

Jianquan Guo: Formal analysis, Data curation, designed the experiments; carried out all the experiments and analyzed the partial data. **Dongsheng Tan:** Formal analysis, Data curation, carried out all the experiments and analyzed the partial data. **Chenmei Lou:** Writing – original draft, designed the experiments; collectively wrote the paper, Formal analysis, Data curation, carried out all the experiments and analyzed the partial data. **Shiying Guo:** Formal analysis, Data curation, contributed to the analysis of the data. **Xing Jin:** Formal analysis, Data curation, contributed to the analysis of the data. **Haijing Qu:** Formal analysis, Data curation, contributed to the analysis of the data. **Lijia Jing:** Writing – original draft, designed the experiments; collectively wrote the paper.

Acknowledgements

This work was financially supported by National Natural Science Foundation of China (No. 81701822), Heilongjiang Province Science Foundation for Youths (No. QC2018090), the Fundamental Research Funds for Central Universities (No. 2572017PZ09). China Postdoctoral Science Foundation (No. 2016M600238), Heilongjiang Postdoctoral Special Fund (No. LBH-TZ1601) and Northeast Forestry University Double First-Rate Construction Fund (No.000/41113281).

Appendix A. Supplementary data

Supplementary data to this article can be found online at https://doi.org/10.1016/j.bioactmat.2021.07.018.

References

[1] C. Holohan, S. Van Schaeybroeck, D.B. Longley, P.G. Johnston, Cancer drug resistance: an evolving paradigm, Nat. Rev. Canc. 13 (2013) 714–726, https://doi.org/10.1038/nrc3599.
[2] G. Szakacs, J.K. Paterson, J.A. Ludwig, C. Booth-Genthe, M.M. Gottesman, Targeting multidrug resistance in cancer, Nat. Rev. Drug Discov. 5 (2006) 219–234, https://doi.org/10.1038/nrd1984.
[3] M.M. Gottesman, T. Fojo, S.E. Bates, Multidrug resistance in cancer: role of ATP-dependent transporters, Nat. Rev. Canc. 2 (2002) 48–58, https://doi.org/10.1038/nrc706.
[4] H.M. Coley, Mechanisms and strategies to overcome chemotherapy resistance in metastatic breast cancer, Canc. Treat Rev. 34 (2008) 378–390, https://doi.org/10.1016/j.ctrv.2008.01.007.
[5] L. Jing, J. Shi, D. Fan, Y. Li, R. Liu, Z. Dai, et al., $^{(177)}$Lu-Labeled cerasomes encapsulating indocyanine green for cancer theranostics, ACS Appl. Mater. Interfaces 7 (2015) 22095–22105, https://doi.org/10.1021/acsami.5b07856.
[6] L. Jing, X. Liang, Z. Deng, S. Feng, X. Li, M. Huang, et al., Prussian blue coated gold nanoparticles for simultaneous photoacoustic/CT bimodal imaging and photothermal ablation of cancer, Biomaterials 35 (2014) 5814–5821, https://doi.org/10.1016/j.biomaterials.2014.04.005.
[7] Q. Chen, J. Wen, H. Li, Y. Xu, F. Liu, S. Sun, Recent advances in different modal imaging-guided photothermal therapy, Biomaterials 106 (2016) 144–166, https://doi.org/10.1016/j.biomaterials.2016.08.022.
[8] L. Wang, X. Lin, J. Wang, Z.J. Hu, Y.L. Ji, S. Hou, Y.L. Zhao, X.C. Wu, C.Y. Chen, Novel insights into combating cancer chemotherapy resistance using a plasmonic nanocarrier: enhancing drug sensitiveness and accumulation simultaneously with localized mild photothermal stimulus of femtosecond pulsed laser, Adv. Funct. Mater. 24 (2014) 4229–4239, https://doi.org/10.1002/adfm.201400015.
[9] Y. Li, Y. Deng, X. Tian, H. Ke, M. Guo, A. Zhu, et al., Multipronged design of light-triggered nanoparticles to overcome cisplatin resistance for efficient ablation of resistant tumor, ACS Nano 9 (2015) 9626–9637, https://doi.org/10.1021/acsnano.5b05097.
[10] S.M. Lee, H.J. Kim, S.Y. Kim, M.K. Kwon, S. Kim, A. Cho, et al., Drug-loaded gold plasmonic nanoparticles for treatment of multidrug resistance in cancer, Biomaterials 35 (2014) 2272–2282, https://doi.org/10.1016/j.biomaterials.2013.11.068.
[11] L. Jing, H. Qu, D. Wu, C. Zhu, Y. Yang, X. Jin, et al., Platelet-camouflaged nanococktail: simultaneous inhibition of drug-resistant tumor growth and metastasis via a cancer cells and tumor vasculature dual-targeting strategy, Theranostics 8 (2018) 2683–2695, https://doi.org/10.7150/thno.23654.
[12] Y. Xing, J. Zhang, F. Chen, J. Liu, K. Cai, Mesoporous polydopamine nanoparticles with co-delivery function for overcoming multidrug resistance via synergistic

chemo-photothermal therapy, Nanoscale 9 (2017) 8781–8790, https://doi.org/10.1039/c7nr01857f.
[13] T. Wang, D. Wang, H. Yu, M. Wang, J. Liu, B. Feng, et al., Intracellularly acid-switchable multifunctional micelles for combinational photo/chemotherapy of the drug-resistant tumor, ACS Nano 10 (2016) 3496–3508, https://doi.org/10.1021/acsnano.5b07706.
[14] P. Baluk, H. Hashizume, D.M. McDonald, Cellular abnormalities of blood vessels as targets in cancer, Curr. Opin. Genet. Dev. 15 (2005) 102–111, https://doi.org/10.1016/j.gde.2004.12.005.
[15] C.G. Willett, Y. Boucher, E. di Tomaso, D.G. Duda, L.L. Munn, R.T. Tong, et al., Direct evidence that the VEGF-specific antibody bevacizumab has antivascular effects in human rectal cancer, Nat. Med. 10 (2004) 145–147, https://doi.org/10.1038/nm988.
[16] Q. Chen, L. Xu, J. Chen, Z. Yang, C. Liang, Y. Yang, et al., Tumor vasculature normalization by orally fed erlotinib to modulate the tumor microenvironment for enhanced cancer nanomedicine and immunotherapy, Biomaterials 148 (2017) 69–80, https://doi.org/10.1016/j.biomaterials.2017.09.021.
[17] S. Wilhelm, A. Tavares, Q. Dai, S. Ohta, J. Audet, F. Harold, C.W. Warren, Analysis of nanoparticle delivery to tumours, Nat. Rev. Mater. 1 (2016) 16014, https://doi.org/10.1039/c9mh00020h.
[18] E. Aarntzen, L. Heijmen, W.J.G. Oyen, 18)F-FDG PET/CT in local ablative therapies: a systematic review, J. Nucl. Med. 59 (2018) 551–556, https://doi.org/10.2967/jnumed.117.198184.
[19] G. He, S. Chen, Y. Xu, Z.H. Miao, Y. Ma, H.S. Qian, Y. Lu, Z.B. Zha, Charge reversal induced colloidal hydrogel acts as a multi-stimuli responsive drug delivery platform for synergistic cancer therapy, Mater. Horiz 6 (2019) 711–716, https://doi.org/10.1039/C9MH00020H.
[20] A. GhavamiNejad, M. SamariKhalaj, L.E. Aguilar, C.H. Park, C.S. Kim, pH/NIR light-controlled multidrug release via a mussel-inspired nanocomposite hydrogel for chemo-photothermal cancer therapy, Sci. Rep. 6 (2016) 33594, https://doi.org/10.1038/srep33594.
[21] Y. Hu, C. Chi, S. Wang, L. Wang, P. Liang, F. Liu, et al., A comparative study of clinical intervention and interventional photothermal therapy for pancreatic cancer, Adv Mater 29 (2017), https://doi.org/10.1002/adma.201700448.
[22] F. Zhang, X. Han, Y. Hu, S. Wang, S. Liu, X. Pan, et al., Interventional photothermal therapy enhanced brachytherapy: a new strategy to fight deep pancreatic cancer, Adv. Sci. 6 (2019) 1801507, https://doi.org/10.1002/advs.201801507.
[23] H. Mizutani, S. Tada-Oikawa, Y. Hiraku, M. Kojima, S. Kawanishi, Mechanism of apoptosis induced by doxorubicin through the generation of hydrogen peroxide, Life Sci. 76 (2005) 1439–1453, https://doi.org/10.1016/j.lfs.2004.05.040.
[24] M.A. Fuertes, J. Castilla, C. Alonso, J.M. Perez, Novel concepts in the development of platinum antitumor drugs, Curr Med Chem Anticancer Agents 2 (2002) 539–551, https://doi.org/10.2174/1568011023353958.
[25] X. Guo, X. Wei, Y. Jing, S. Zhou, Size changeable nanocarriers with nuclear targeting for effectively overcoming multidrug resistance in cancer therapy, Adv Mater 27 (2015) 6450–6456, https://doi.org/10.1002/adma.201502865.
[26] L. Pan, J. Liu, Q. He, J. Shi, MSN-mediated sequential vascular-to-cell nuclear-targeted drug delivery for efficient tumor regression, Adv Mater 26 (2014) 6742–6748, https://doi.org/10.1002/adma.201402752.
[27] L. Pan, Q. He, J. Liu, Y. Chen, M. Ma, L. Zhang, et al., Nuclear-targeted drug delivery of TAT peptide-conjugated monodisperse mesoporous silica nanoparticles, J. Am. Chem. Soc. 134 (2012) 5722–5725, https://doi.org/10.1021/ja211035w.
[28] G. Qi, Y. Zhang, S. Xu, C. Li, D. Wang, H. Li, et al., Nucleus and mitochondria targeting theranostic plasmonic surface-enhanced Raman spectroscopy nanoprobes as a means for revealing molecular stress response differences in hyperthermia cell death between cancerous and normal cells, Anal. Chem. 90 (2018) 13356–13364, https://doi.org/10.1021/acs.analchem.8b03034.
[29] W. Chen, J. Liu, Y. Wang, C. Jiang, B. Yu, Z. Sun, et al., A C5 N2 nanoparticle based direct nucleus delivery platform for synergistic cancer therapy, Angew Chem. Int. Ed. Engl. 58 (2019) 6290–6294, https://doi.org/10.1002/anie.201900884.
[30] Y. Cao, T. Wu, K. Zhang, X. Meng, W. Dai, D. Wang, et al., Engineered exosome-mediated near-infrared-II region V2C quantum dot delivery for nucleus-target low-temperature photothermal therapy, ACS Nano 13 (2019) 1499–1510, https://doi.org/10.1021/acsnano.8b07224.
[31] S. Venkatesh, J.L. Workman, Histone exchange, chromatin structure and the regulation of transcription, Nat. Rev. Mol. Cell Biol. 16 (2015) 178–189, https://doi.org/10.1038/nrm3941.
[32] T. Kouzarides, Chromatin modifications and their function, Cell 128 (2007) 693–705, https://doi.org/10.1016/j.cell.2007.02.005.
[33] Z. Yang, R. Cheng, C. Zhao, N. Sun, H. Luo, Y. Chen, et al., Thermo- and pH-dual responsive polymeric micelles with upper critical solution temperature behavior for photoacoustic imaging-guided synergistic chemo-photothermal therapy against subcutaneous and metastatic breast tumors, Theranostics 8 (2018) 4097–4115, https://doi.org/10.7150/thno.26195.
[34] L. Jing, C. Shao, Y. Wang, Y. Yang, X. Yue, Z. Dai, Hyaluronic acid modified hollow prussian blue nanoparticles loading 10-hydroxycamptothecin for targeting thermochemotherapy of cancer, Theranostics 6 (2016) 40–53, https://doi.org/10.7150/thno.13250.
[35] Y. Yang, W. Zhu, Z. Dong, Y. Chao, L. Xu, M. Chen, et al., 1D coordination polymer nanofibers for low-temperature photothermal therapy, Adv. Mater. 29 (2017), https://doi.org/10.1002/adma.201703588.
[36] S. Miura, H. Suzuki, Y.H. Bae, A multilayered cell culture model for transport study in solid tumors: evaluation of tissue penetration of polyethyleneimine based cationic micelles, Nano Today 9 (2014) 695–704, https://doi.org/10.1016/j.nantod.2014.10.003.
[37] H. Suzuki, Y.H. Bae, Evaluation of drug penetration with cationic micelles and their penetration mechanism using an in vitro tumor model, Biomaterials 98 (2016) 120–130, https://doi.org/10.1016/j.biomaterials.2016.04.037.
[38] D. Shechter, H.L. Dormann, C.D. Allis, S.B. Hake, Extraction, purification and analysis of histones, Nat. Protoc. 2 (2007) 1445–1457, https://doi.org/10.1038/nprot.2007.202.